Experimental Analysis of Cylindrical Wave Fields

Experimental Analysis of Cylindrical Wave Fields

J. Cameron McNatt
Institute for Energy Systems, The University of Edinburgh
Edinburgh, Scotland, UK
E-mail: c.mcnatt@ed.ac.uk

Vengatesan Venugopal
Institute for Energy Systems, The University of Edinburgh
Edinburgh, Scotland, UK
E-mail: v.venugopal@ed.ac.uk

David I. M. Forehand
Institute for Energy Systems, The University of Edinburgh
Edinburgh, Scotland, UK
E-mail: d.forehand@ed.ac.uk

Grégory S. Payne
Institute for Energy Systems, The University of Edinburgh
Edinburgh, Scotland, UK
E-mail: gregory.payne@ed.ac.uk

Abstract—In a previous theoretical paper submitted to EWTEC, the authors showed that the wave energy converter (WEC) wave field can be accurately and analytically represented by cylindrical linear waves with the appropriate coefficients. In that paper, the coefficients were found computationally using the boundary-element method software, WAMIT. For the present paper, experiments were conducted in the newly refurbished University of Edinburgh Curved Wave Tank to determine the same cylindrical coefficients for progressive waves. The experiments employed two body geometries, an attenuator consisting of a horizontal pitching cylinder, and a terminator made up of a bottom-hinged flap. An array of 59 wave gauges was arranged in a circle-spoke pattern, where the circle of wave gauges was necessary for deriving the cylindrical coefficients, and the spokes, which extended radially further afield, were used for validation. Both the scattered and the radiated waves of the bodies were examined at three frequencies. High-order harmonics were present in a number of the wave fields, and tank reflections were problematic. Despite this, the linear analytical wave field, whose coefficients were found experimentally, agrees well with the experimentally measured linear wave field at points other than those used to derive the coefficients. The results serve to validate linear wave theory as it relates to the wave field and reinforce the concept that these waves can be used to compute WEC performance and wave farm interactions and impacts.

I. Introduction

To design a wave energy converter (WEC), scientists and engineers need to have comprehensive understanding of the wave field and how it is modified by a WEC. To effectively absorb power, a WEC needs to radiate waves that cancel the diffracted wave field. The wave absorption, scattering, and radiation of the WEC are the means of multi-body interactions in a wave farm, and modification of the wave field will have environmental impacts.

For heaving and surging point absorbers, Wypych et al. [1] showed that circular-cylindrical radiated waves destructively interfere with the outwardly propagating portion of the incident wave, canceling it out and absorbing energy. McNatt et al. [2] use the cylindrical wave fields of floating bodies with a method developed by Kagemoto and Yue [3] to efficiently compute hydrodynamic interactions between multiple bodies in a large wave farm. Several studies have used phase-averaged models (e.g. [4]) or phase-resolving models (e.g. [5]) to

examine the effects of a wave farm on the environment. However, as suggested by Babarit [6], more work needs to be done on how to effectively represent the wave field of a floating body in a phase-averaged wave model.

In cylindrical form, a wave field is described as the superposition of various orders of progressive and evanescent cylindrical wave modes that are modified by complex coefficients. The challenge is to determine the amplitude and phase of the coefficients. In a 2013 EWTEC paper, McNatt et al. [7] (also published here [8]) described a method for computing the cylindrical coefficients by making "measurements" of the wave field around a body over a circular-cylindrical control surface that extends from the bottom to the free-surface. They then demonstrated the method computationally with the linear boundary-element software, WAMIT, and found excellent agreement of the cylindrical wave field with ones computed entirely by WAMIT. The method is generic and it was suggested therein that it could be applied experimentally.

Here, wave tank experiments are described, which attempted to experimentally apply the method of finding the cylindrical coefficients described in McNatt et al. [8]. The experiments were conducted in the University of Edinburgh Curved Tank. An array of 59 wave gauges was arranged in a "circle-spoke" pattern, where the circle of wave gauges was necessary for deriving the cylindrical coefficients, and the spokes, which extended radially further afield, were used for validation. Two simple body geometries, each with a single degree-of-freedom (DOF) were considered: a "Flap" (or terminator), and an "Attenuator". Tests were conducted with each body in forced harmonic motion to measure the radiated wave. The wave field was also measured in the absence of the body to find the incident wave field, and with each body held fixed to find the diffracted wave field. The difference of these two produced the scattered wave field.

Results are shown for the measured wave field, the cylindrical wave field where the coefficients were produced from the experimental measurements, and for a cylindrical wave field where the coefficients were found in WAMIT. In many cases the cylindrical wave field produced from measurements is a good representation of the complete measured wave field, and

is almost always better than that produced by the WAMIT model. However, there were two issues: 1) the waves were not completely linear, and to varying degrees, higher-order harmonics were present; and 2) reflections of the radiated and scattered waves off the tank walls and paddles degraded the match and most likely caused errors in the cylindrical coefficients, which may have been significant in some cases. Overall though, results were very good, and serve to validate the cylindrical wave representation of the wave field of floating bodies.

II. THEORY

The theory given here briefly describes the cylindrical wave field coefficients, how they are used to create an analytical wave field and how they were estimated experimentally. Linear wave theory is assumed. The fluid is incompressible, inviscid and irrotational. Wave amplitudes and body motions are small perturbations about a mean value and are harmonic with time. The fluid velocity is the gradient of a velocity potential: $\boldsymbol{V}(\boldsymbol{x}, t) = \mathrm{Re}\left\{\nabla\phi(\boldsymbol{x})e^{\mathrm{i}\omega t}\right\}$, where $\phi(\boldsymbol{x})$ depends only on spatial coordinates, $\boldsymbol{x}$; $\mathrm{i} = \sqrt{-1}$; ω is the circular frequency and t is time. The governing equation of the boundary-value problem (BVP) is Laplace's equation: $\nabla^2\phi = 0$. The boundaries are the linearized free surface, a flat bottom, the impenetrable boundaries of any bodies present, and in some cases a radiation condition. The full linear wave-body boundary value problem shall not be given here, and can be found for example in Newman [9]. More information on the cylindrical solution and the theory given here can be found in McNatt et al. [8].

The wave elevation, $\eta(\boldsymbol{x})$, is a complex amplitude as function of space and is independent of time. It is related to the velocity potential by $\eta = -\frac{\mathrm{i}\omega}{g}\phi|_{z=0}$. The wave field of a body (or multiple bodies) in waves is given as

$$\eta = \eta^I + \eta^S + \sum_{i=1}^{Q}\zeta_i\eta_i^R \tag{1}$$

where, η^I is the incident wave elevation, η^S is the scattered wave elevation, ζ_i is the complex amplitude of the ith mode of motion, η_i^R is the unit amplitude elevation of the ith mode of motion and Q is the total number of degrees of freedom. Solutions to the BVP solved in cylindrical coordinates, $\{r, \theta, z\}$ for the scattered and radiated wave elevation are of the form:

$$\eta^{S,R}(r, \theta) = \sum_{m=-\infty}^{\infty} a_m H_m^{(2)}(kr)e^{\mathrm{i}m\theta} \tag{2}$$
$$+ \sum_{l=1}^{\infty}\sum_{m=-\infty}^{\infty} a_{lm}\cos(k_l h)K_m(k_l r)e^{\mathrm{i}m\theta}$$

where the first set of terms, $a_m H_m^{(2)}(kr)e^{\mathrm{i}m\theta}$ represents cylindrical waves that propagate away from the origin. a_m is the mth complex cylindrical coefficient; $H_m^{(2)}(kr)$ is the mth order Hankel function of the second kind; k is the progressive wave number. The second set of terms,

$a_{lm}\cos(k_l h)K_m(k_l r)$, represent the evanescent wave modes. a_{lm} is the lm^{th} complex evanescent cylindrical coefficient; k_l is the lth evanescent wave number; h is the water depth; and $K_m(k_l r)$ is the mth modified Bessel function of the second kind.

Equation 2 is a full analytical description of the scattered or radiated wave elevation. The coefficients a_m and a_{lm} are generally not given by off-the-shelf software. McNatt et al. [8] described a method for finding these coefficients by taking "measurements" of the velocity potential over a circular cylindrical control surface that circumscribes the body. In that method, the control surface needed to extend from the bottom to the free surface in order to isolate the evanescent modes. In software, making such measurements is straightforward.

However, experimentally it would be difficult to accurately measure a sufficient number of points in the vertical direction. Accurate measurements with wave gauges of the wave elevation can reliably be made, but knowing the wave field only at $z = 0$, it is not possible to isolate the progressive coefficients, a_m from the evanescent coefficients, a_{lm}. However, evanescent waves decay very quickly with radial distance. If one extends the radius of the circle of measurement points to a sufficient distant from the body, one may assume that the evanescent wave amplitudes are negligible, and that the wave elevation is given as:

$$\eta^{S,R}(r, \theta) \simeq \sum_{m=-\infty}^{\infty} a_m H_m^{(2)}(kr)e^{\mathrm{i}m\theta} \tag{3}$$

If one knows the wave elevation over a circle of radius, r_0, where r_0 is sufficiently large enough to neglect evanescent wave modes, the mth cylindrical coefficient can be found using a Fourier transform as:

$$a_m = \frac{1}{2\pi}\frac{1}{H_m^{(2)}(kr_0)}\int_0^{2\pi}\eta(r = r_0, \theta)e^{-\mathrm{i}m\theta}d\theta \tag{4}$$

III. EXPERIMENTAL DESIGN

The experiments were designed to measure the wave elevation, so as to derive the cylindrical coefficients and test the analytical representation of the wave field. Critical to this analysis is the design of a wave gauge array. Furthermore, the scattered and radiated coefficients need to be derived separately, and so multiple experimental setups were devised to do this. For variety, the analysis was performed on two different WEC-like geometries: a "flap" (also known as a "terminator") and an "attenuator" for three wave frequencies: 0.8, 1, and 1.25 Hz.

A. Wave Tank

The experiments were conducted in The University of Edinburgh Curved Wave Tank. The tank was refurbished in May-June 2014, shortly before the experiments were conducted in October-November, 2014. Prior to the refurbishment, the performance of the tank was analyzed in Gyongy et al. [10]

a) Tank with wave gauges
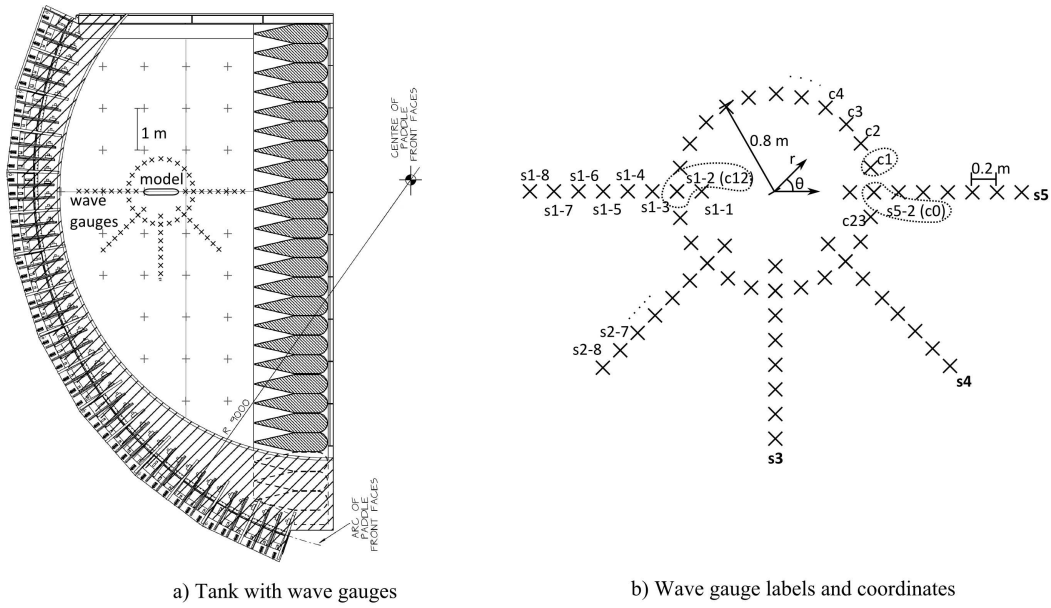
b) Wave gauge labels and coordinates

Fig. 1. The figures show the experimental test setup including a) the location of wave gauges in the wave tank, and b) the wave gauges with their coordinate system and labels.

in order to validate a computational model of the tank. The tank (see Figure 1-a) has a curved array of force-feedback absorbing wave makers subtending an arc of 96 degrees at a radius of 9 m. Opposite the wave makers is a 12 m length of "beaches" made up of porous material, and along one side is a glass wall of length 4.4 m. The wave makers are capable of generating waves over a frequency range of 0.5-1.5 Hz. The water depth at which the tests were performed was 1.16 m.

B. Wave Measurements

The wave gauge array consisted of a circle of 24 wave gauges, and 5 spokes of 8 wave gauges each. Measurements from the circle of gauges are used to find the cylindrical coefficients via Equation 4, and measurements along the spokes are used to validate the analytical wave field given by Equation 3. The array is shown in Figure 1 in a schematic of the curved tank as well as close up with its coordinates and labels. The center of the circle was taken to be the origin of the wave gauge array. The directional coordinate, θ, was defined so that $\theta = 0$ corresponded to the $\beta = 0$ incident wave direction of the tank, which was also parallel to the tank's glass wall. Positive θ is counter-clockwise.

The circle of wave gauges was positioned at a radius of $0.8\,m$, and were numbered $c0 - c23$ over even increments in θ of $\pi/12$ radians. The spokes extended radially along constant θ. They were numbered $s1 - s5$, and along each spoke were 8 wave gauges, numbered for example: $s1 - 1$, $s1 - 2, \ldots$ going radially outward. The $s1$ spoke was located at $\theta = \pi$, $s2$ at $\theta = \frac{5}{4}\pi$, $s3$ at $\theta = \frac{3}{2}\pi$, $s4$ at $\theta = \frac{7}{4}\pi$, and $s5$ at $\theta = 0$. The spacing between gauges along the spokes was $0.2\,m$, and the first gauge was located at $r = 0.6\,m$. Five of the wave gauges were part of both the circle and the spokes; these were in the 2 position of the spokes (e.g. $s1 - 2$). The total number of wave gauges employed was 59.

The gauges were resistive wave gauges. They were made up of two $3mm$ diameter stainless steel round bars with a working length of $0.3\,m$ and a separation distance of $20\,mm$. The wave gauges were wired to one of 3 older model Wave Gauge 8 measurement boxes by Edinburgh Designs. Only 3 wave gauge boxes were available, each box had only 8 measurement channels, and one box had two broken channels, which meant that only 22 wave gauge channels were active for any given run. Consequently, each test was performed 3 times in order to capture all of the wave gauge information.

Calibration is a very important aspect of using wave gauges. Calibrating 59 wave gauges could be arduous, however, a novel calibration system was devised which allowed all the active wave gauges to be calibrated simultaneously. The entire wave gauge rig was supported by two beams that spanned the tank from the wave maker side to the beach side (see Figure 2). Each end of each beam was supported by a car scissor jack, next to which was a ruler. The entire rig could be raised and lowered by a known amount by adjusting these scissor jacks, which would in turn raise or lower the wave gauges in the tank. It was estimated that the rig could be set to a vertical accuracy of less than $0.5\,mm$.

A five point calibration over a range of $\pm 40\,mm$ was used for each gauge, and the gauges were found to be very linear. The wave gauges were calibrated at least everyday, or multiple times per day if the active wave gauges were switched.

A calibrated wave gauge measures wave elevation as a function of time. The wave signal was periodic, but not necessarily sinusoidal (i.e. linear). For the theory, the complex linear amplitude is needed. To extract the amplitude, an FFT
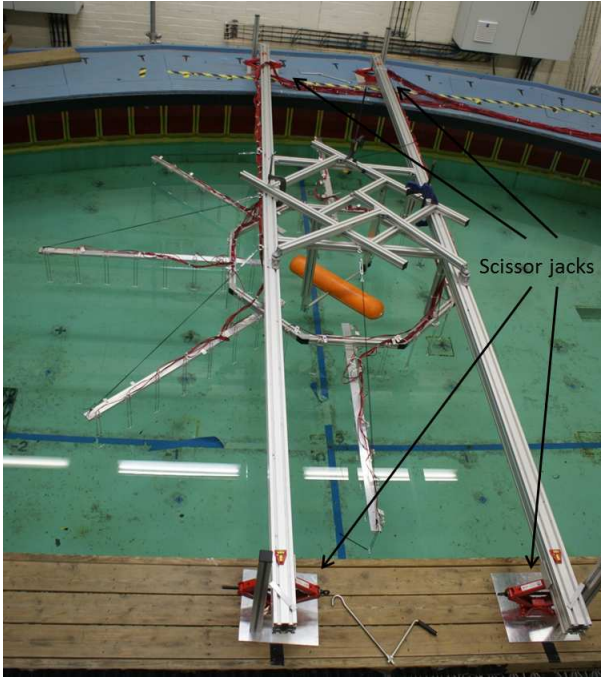
Fig. 2. The picture shows the experimental setup in the wave tank. One can see the two cross-beams which support the wave gauges and model from overhead. The scissor jacks which were used to calibrate the wave gauges are indicated. The model is the attenuator at an orientation of $45°$.

a) Flap   b) Attenuator

Fig. 3. The diagram shows the bodies indicating specifically the location of the hinge and the mode of motion.

a) Flap   b) Attenuator

Fig. 4. Shown are drawings of each geometry model assembly indicating dimensions in meters.

was performed on the time domain signal of each wave gauge, after a point in time when the waves appeared to have reached a steady state. Then the amplitude and phase of the lowest order signal, which always conformed to the frequency of interest was used for the complex linear amplitude. Care was taken to ensure that an integer number of periods were present in the measurement window so as to produce a frequency domain signal with very little leakage.

C. Physical Models

Two different types of WEC models were used in the analysis: a "flap" and an "attenuator" [11]. Each only had a single degree of freedom. The flap was hinged at the bottom and can be thought of as a terminator because its across-wave dimension was significantly larger that its along-wave dimension. The attenuator was a horizontal cylinder with spherical ends that pitched about its midpoint, which was located at the still water level. The single degree of freedom was maintained through hinges that were fixed to a frame mounted on beams that were suspended above the water. Figures 3-a) and -b) show a diagram of the flap and attenuator and indicate each ones mode of motion. Figure 2 shows the attenuator in its setup.

Figures 4-a) and -b) show the dimensions of the flap and attenuator. The flap had a width of $0.6\,m$, a height of $0.5\,m$, a thickness of $0.08\,m$, and a draft of $0.4\,m$. The corners and edges were rounded slightly to reduced viscous effects. The attenuator had an overall length of $0.8\,m$, and a diameter of $0.16\,m$. The ends where hemispherical, and it was half
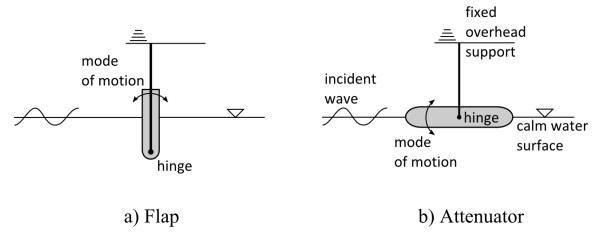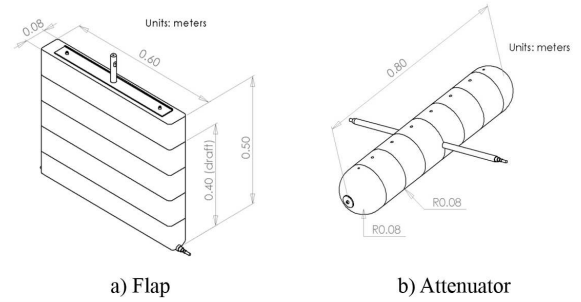
submerged in still water. The models were constructed of a high-performance foam called Divinycell around an internal aluminium frame.

The physical setup also allowed the body orientation to be changed relative to the wave gauge coordinate system to achieve different incident wave directions. Two body orientations were considered: $0°$ and $45°$ (incident direction of $-45°$), where the orientation is a rotation of the body in the θ coordinate. See Figures 1-b and 2.

The models were not true WECs as they did not intentionally absorb wave power - there was no power-take-off (PTO) mechanism. This approach was taken, because a PTO was not necessary to the analysis, and the lack of one reduced the complexity of the physical model design.

D. Run Conditions

Three frequencies were considered for the tests: 0.8, 1, and 1.25 Hz. Plane waves were used as the incident waves, and for some conditions the body was rotated to change the incident wave angle. At each frequency, three tests were performed: incident, diffracted, and radiated. Each test was repeated at least twice, then the mean of the linear amplitude and mean of the linear phase was taken as the final result.

1) Incident, η^I: For this, a plane wave at each frequency was measured with no body present, it is represented by the wave elevation: η^I.

2) Diffracted, $\eta^I + \eta^S$: For these tests, the models were fixed in their mean position and subjected to incident waves. The diffracted wave field is the sum of the incident and the scattered wave fields: $\eta^I + \eta^S$, and so the scattered wave field was then found by subtracting the incident from the diffracted.
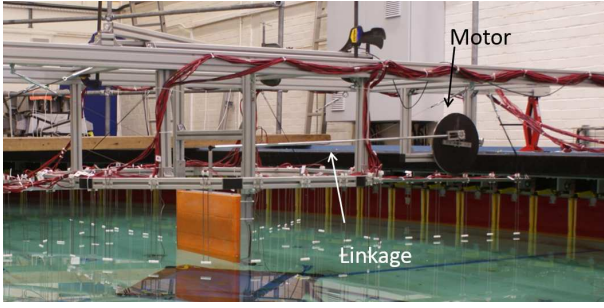
Fig. 5. The picture shows the radiated wave setup for the flap. Indicated are the motor (one sees the steel wheel used as inertia) and the linkage to the body, which was designed to be long compared to the amplitude of motions. As shown the setup is not in its running position, but is raised out of the water.
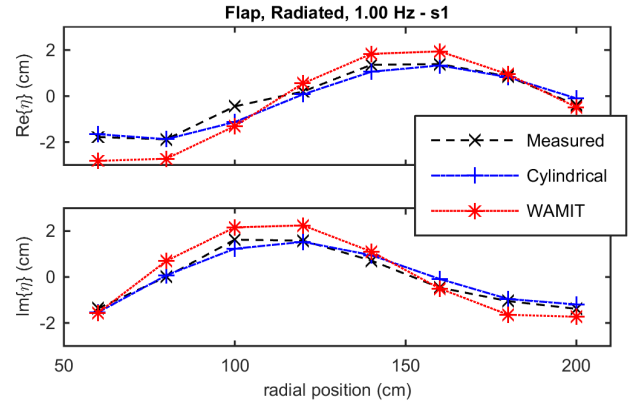

Fig. 6. The figure shows the real and imaginary parts of the linear amplitude, which indicates the phase alignment, of spoke $s1$ for Flap in the radiated wave setup at 1 Hz. The full result is shown in Figure 8.

That is, the difference of the complex linear amplitudes was taken between the diffracted and the incident wave fields to get the scattered wave field. The diffracted wave field was computed for two body orientations: $0°$ and $45°$. For both the incident and diffracted wave conditions, the start of the measurements was triggered by a signal from the wave makers, which ensured a phase coherence between the incident and diffracted wave measurements as well as between repeated tests.

3) Radiated, $\zeta\eta^R$: The radiated wave field was created by forcing a harmonic motion on the body in its degree of freedom in the absence of incident waves. The radiated wave field is described by $\zeta\eta^R$, where η^R is the unit amplitude wave field and ζ is the complex motion amplitude. The harmonic forcing was produced by driving the motion with a linkage connected to a cam, which was connected to a motor. To produce a sinusoidal motion in angle, the linkage was designed to be long with respect to the lever arm on the body and the radius of the cam. Figure 5 shows the radiated wave setup for the terminator.

The motor was run open loop to simplify the setup. A large steel plate was used as an inertial mass to help maintain a harmonic motion. However, it was difficult to tune the motion exactly to the frequency of interest, and the motion drifted slightly in amplitude and frequency. In the radiated wave field tests, the drive frequency was off by a maximum of 2% of the desired frequency, which would result in approximately a 4% error in wavelength.

The motion of the body, ζ, was measured with a waterproof contactless sensor that was connected at the hinge location. The total radiated wave, $\zeta\eta^R$, was measured by the wave gauges. There was no mechanism for triggering the measurements, and so measurements made by repeat tests were aligned in phase, by normalizing the wave phase to the phase of the body position.

E. Experimental Data Repository

All the experimental data from these tests, including raw data, setup descriptions, pictures and videos, and Matlab scripts is available for free online: github.com/

camalamadingdong/cyl_wfe. The authors hope that the data can be useful to other scientists and engineers.

IV. RESULTS AND DISCUSSION

Results are shown in Figures 8-10 for a selection of conditions: the flap radiated wave field at 1 Hz, the flap oriented at $0°$ scattered wave field at 0.8 Hz, and the attenuator oriented at $45°$ scattered wave field at 1.25 Hz. The results were selected to show some of the best and worst matches as well as cover all frequencies.

The plots show three lines:

Measured:
>   Magnitude of the linear wave amplitudes from tank measurements

Cylindrical:
>   Magnitude of the wave amplitudes predicted by Equation 3, where the cylindrical coefficients were computed from the measurements via Equation 4

WAMIT:
>   Magnitude of the wave amplitudes predicted by Equation 3, where the cylindrical coefficients were computed with WAMIT, see [8]

The top plots show the points around the circle of wave gauges, where the abscissa is angular position. Plots along the left-hand side show the spokes of wave gauges. For the scattered results, the magnitude of the incident wave, $|\eta^I|$, is given, which was taken as the mean of the magnitudes of all wave gauges. For the radiated wave results, the magnitude of the angle of motion, $|\zeta|$, is give.

Also shown in each figure are the magnitudes of the cylindrical coefficients, $|a_m|$, as a function of m, and the magnitude of the Kochin function, $|F(\theta)|$, of the radiated or scattered wave. The Kochin function describes the far-field wave field by: $\eta_f^{S,R} = F(\theta)(kr)^{-1/2}e^{-ikr}$, and is related to the cylindrical coefficients by: $F(\theta) = \sqrt{\frac{2}{\pi}}e^{i\frac{\pi}{4}}\sum e^{im\frac{\pi}{2}}a_m e^{im\theta}$.

The R^2 value for both the Cylindrical (R_C^2) and the WAMIT (R_W^2) data is given, where: $R^2 = 1 - $

Body	Wave	Orient (deg)	Freq (Hz)	R_C^2	R_W^2
Flap	Radiated	-	0.8	0.78	0.68
			1	0.95	0.80
			1.25	0.90	0.78
	Scattered	0	0.8	0.93	0.91
			1	0.97	0.89
			1.25	0.91	0.80
		45	0.8	0.86	0.80
			1	0.92	0.84
			1.25	0.91	0.84
Attenuator	Radiated	-	0.8	0.60	0.61
			1	0.75	0.79
			1.25	0.86	0.86
	Scattered	0	0.8	0.68	0.64
			1	0.76	0.70
			1.25	0.75	0.74
		45	0.8	0.68	0.56
			1	0.82	0.57
			1.25	0.35	0.18

TABLE I

THE R^2 VALUES FOR THE CYLINDRICAL FIT TO THE DATA (R_C^2) AND FOR THE WAMIT FIT TO THE DATA (R_W^2) FOR EACH CONDITION.

Fig. 7. Figure shows plots of the full run-time time series, amplitude spectra, and close-up of the time series for wave gauge c12 (also s1-2) for both the diffracted and radiated wave field of the Flap at 1 Hz.

$\sum (y_i - f_i)^2 / \sum (y_i - \bar{y})^2$, and y_i is the measured data point, f_i is the Cylindrical or WAMIT point, and $\bar{y}$ is the mean of the measurements. The R^2 value indicates how well a model fits a given set of data relative the variance of the data, where a value closer to 1 indicates a better fit. R^2 was computed using only the data points along the spokes; the points over the circle are neglected, because this is where the Cylindrical values were fitted to the measurements originally. The R^2 values for all cases are summarized in Table I.

Although the plots only show the magnitude of the wave amplitudes, the R^2 also takes into account the phase difference. Equation 3, of course, models both the amplitude and the phase. When results are plotted as $\text{Re}\{\eta\}$ (or $\text{Im}\{\eta\}$) which shows the phase of the wave, the match between the Measurements and the Cylindrical model is more striking, as can be seen in Figure 6, which shows the Flap radiated wave at 1 Hz along spoke s1.

Figure 8 shows the results from the Flap radiating at 1 Hz. Around the circle of gauges, the Cylindrical results and the Measured results are virtually indistinguishable. In a way, this should not be surprising as the Cylindrical results are fitted around this circle with a Fourier transform. However, they do not necessarily match everywhere as the Cylindrical results are produced with 11 cylindrical (Fourier) coefficients (a truncation value of $M = 5$), which may not be sufficient to reproduce the circle Measurements exactly. However, in this case, the Flap produces a very nice clean "Pitch" type radiated wave - a wave that has one phase on the front of the body and the opposite phase in the back. This type of wave is dominated by the $|m| = 1$ cylindrical coefficients. In Figure 8, the $m = \pm 1$, a_m, coefficients are dominant, while the other a_m coefficients are nearly 0. Comparison of the Cylindrical to the Measured out along the spokes is also very good, and here is where the judgment of the Cylindrical should be made - that is, the Cylindrical was devised from measurements around the circl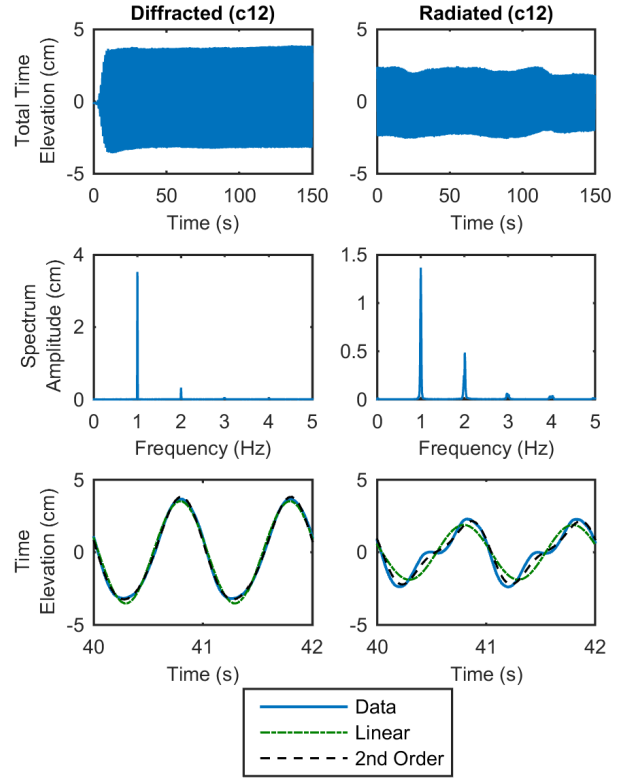e, and comparison along the spokes shows the goodness-of-fit of Equation 3, where the coefficients are computed with Equation 4. There is some disagreement at the far ends of the spokes, but generally the trend of the Cylindrical matches the Measured well.

Comparison of the WAMIT modeled results shows that WAMIT over estimates the magnitude of the measured linear radiated wave. However, WAMIT does accurately predict the "Pitch" wave behavior, and it shows the correct trends in magnitude and phase. One explanation for WAMIT's over-estimate is that the measurements shown in the plots are of the linear amplitudes, and in almost all cases, higher order harmonics were present, which WAMIT does not model. That is, for a given motion, WAMIT models the wave that is generated as completely linear, whereas in physical reality, some of the wave energy is in higher-order harmonics and the measurements given here only show the linear portion.

Figure 7 shows plots of the full run-time time series, amplitude spectra, and close-up of the time series for wave gauge c12 (also s1-2) for both the diffracted and radiated wave field of the Flap at 1 Hz. Firstly, as mentioned, higher-order component are present. For the diffracted case, the second order component (the spike in the amplitude spectrum at 2 Hz) has an amplitude which is about about 9.1% of the linear component, which is only 0.8% by energy. (Energy is proportional to amplitude squared.) For the radiated case, which is the case considered in Figure 8, the amplitude of the
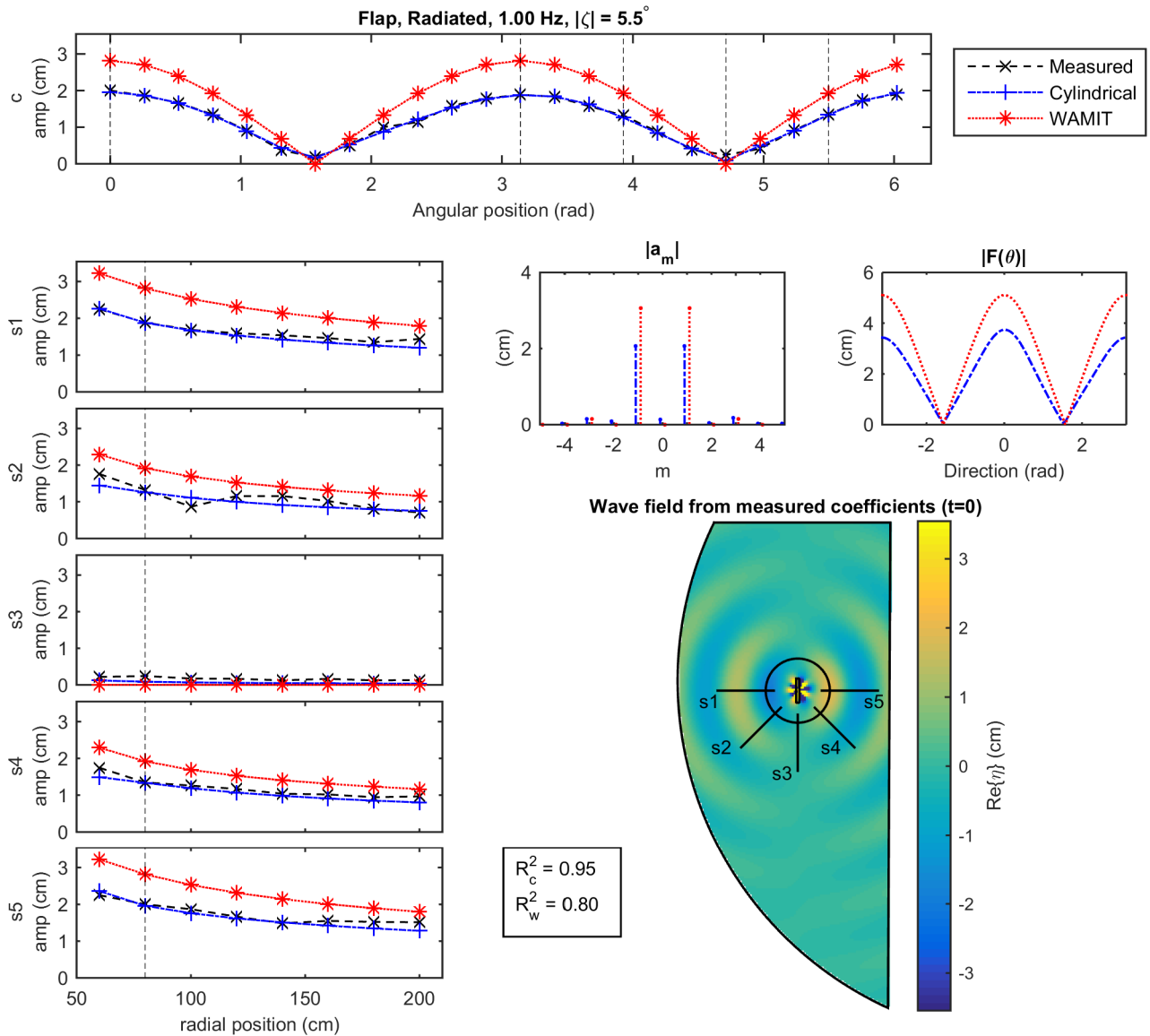
Fig. 8.   The figure shows the results for the Flap radiated wave tests at 1 Hz.

second order harmonic is 32% of the primary, which means that it has about 10% of the energy, a fairly significant value. The plots at the bottom show a close up of the time-domain signal, and one can see that the "2nd order" fit, which is the sum of the sinusoidal signal at the primary frequency and one at the second order frequency, does improve the fit to the data. For the diffracted case, it improves it only marginally, while for the radiated it makes a significant difference.

Although the second order portion is significant in the radiated wave field, the cylindrical theory given herein only applies to linear waves, and so the second order component cannot be addressed. This partially explains the disagreement between WAMIT and the Measured data. For example, at that wave gauge (c12), WAMIT predicts an amplitude of 2.8

cm, while the linear measured amplitude is only 1.9 cm, a difference of 50%.

Also here, it is important to note that the radiated wave signal is not as clean as the diffracted signal - the amplitude of the time-domain signal varies with time, the spectrum has a bit of what looks like leakage around the frequency peaks, and the close up of the time-domain signal show a fairly nonlinear wave. These issues were not necessarily intrinsic to the radiated wave with this body, but more likely due to the experimental setup. As was mentioned in Section III-D, the motor was driven open loop and it was difficult to maintain its precision. If the experiments were to be repeated, it would be a good idea to have feedback control on the motor. In the amplitude spectrum, the spreading around the peaks is not
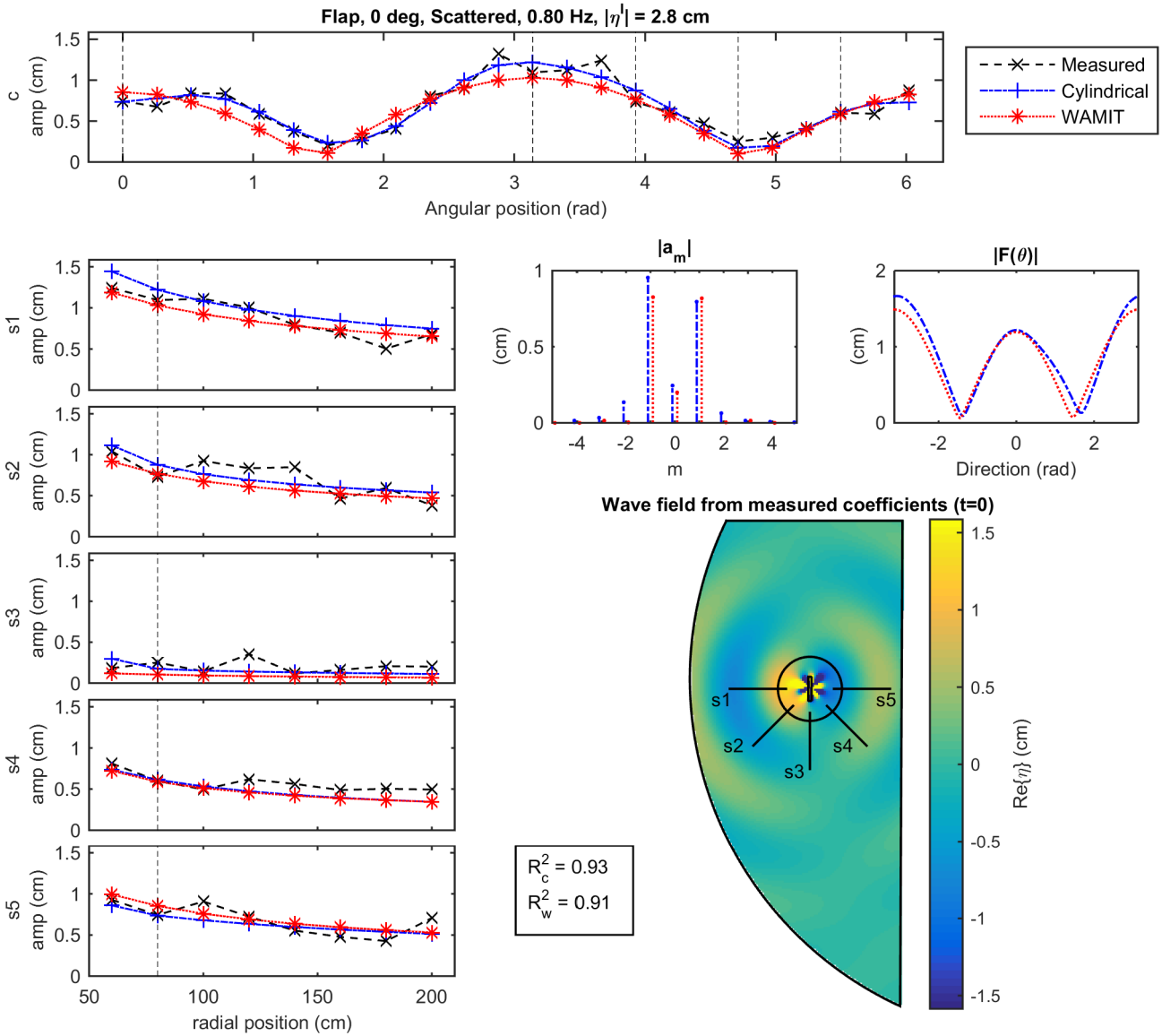
Fig. 9. The figure shows the results for the Flap scattered wave tests at 0.8 Hz.

"leakage" as the result of signal processing, but a real result due to a slight variation in the drive frequency of the motion over time. Because of this spreading, the sum, rather than a single peak, of all complex amplitudes with energy near each peak was used to produce the linear amplitudes and phases.

Figure 9 shows results for the scattered wave of the Flap oriented at $0°$ for a wave with $0.8 Hz$. The Cylindrical is not as exact around the circle as it was for the radiated wave case, and going out along the spokes, one sees some slight oscillations in the measured data that are not present in the Fit or WAMIT. These oscillations are standing waves due to reflections of the scattered wave off of the wave tank walls and paddles. The reflections are not of the incident wave, because the total incident wave field, which includes reflections is subtracted

out when the difference is taken between the diffracted and the incident waves.

Equation 3, which is used to represent the Cylindrical and WAMIT wave field, only describes outwardly propagating waves, that is, the Hankel function of the second kind, $H_m^{(2)}(kr)$, describes outwardly propagating wave energy. There is no mechanism to represent incident wave energy, such as reflections that would produce the oscillations in magnitude that are standing waves. In cylidrical coordinates, incident waves are described using a Bessel function of the first kind, $J_m(kr)$. An arbitrary incident wave is: $\eta^I = \sum_{m=-\infty}^{\infty} a_m^I J_m(kr) e^{im\theta}$. Like with the outgoing radiated and scattered wave fields, the directionality of the incident wave field is embedded in the cylindrical coefficients.
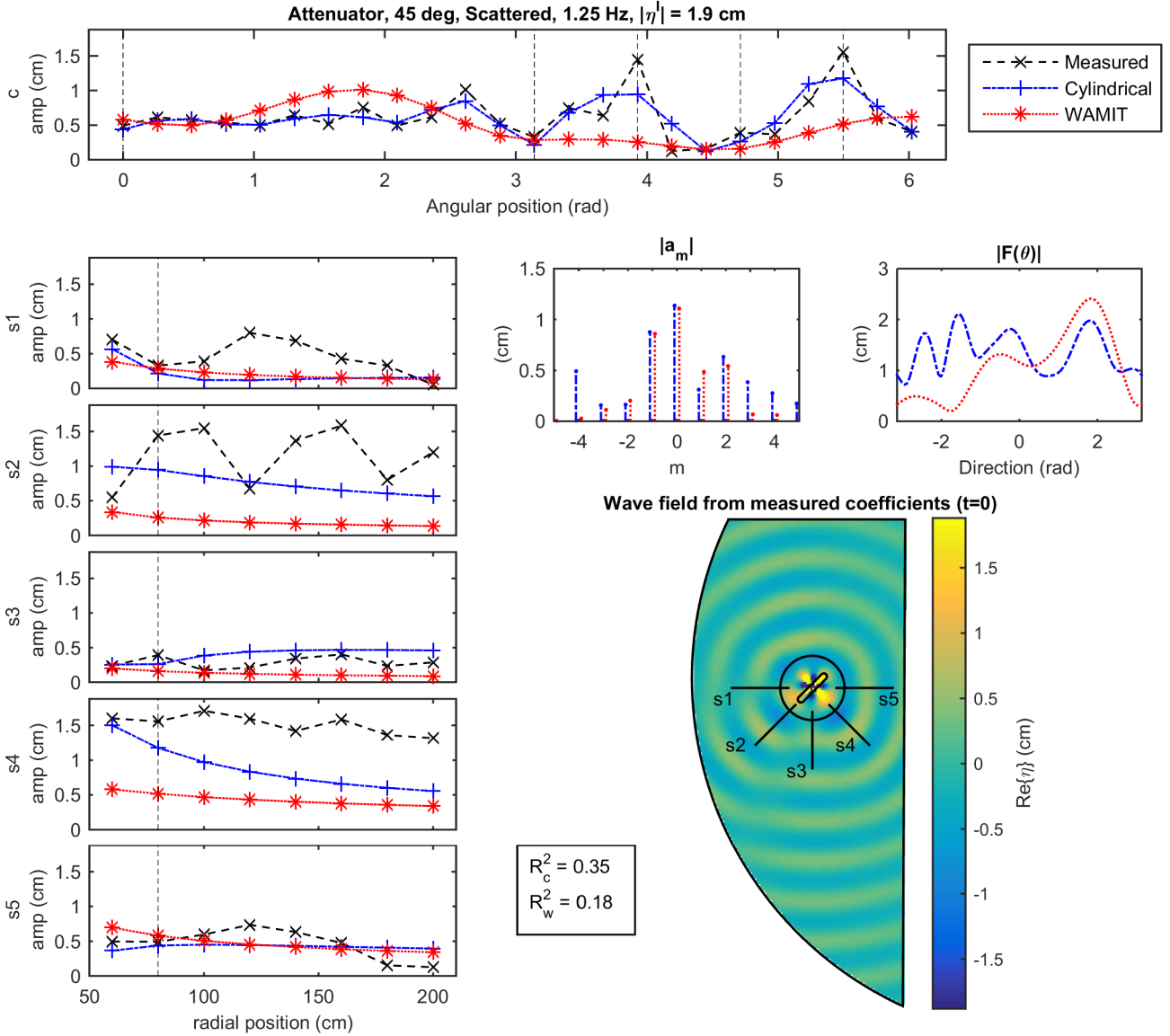
Fig. 10. The figure shows the results for the Attenuator scattered wave tests at 1.25 Hz.

However, a complex function describing the direction of the incident waves can be found: $a(\beta) = \sum_{m=-\infty}^{\infty} e^{im\frac{\pi}{2}} a_m^I e^{im\beta}$, where β is the "plane wave direction". See John [12], Section 5, although his expression for the directional function (5.23) lacks the $e^{im\frac{\pi}{2}}$ coefficient, it is accounted for in next equation by the use of $\theta - \frac{\pi}{2}$ as the argument of his $g()$ function.

The actual linear wave field including the outwardly propagating radiated and scattered waves as well as the reflections should be described as:

$$\eta = \sum_{m=-\infty}^{\infty} \left(\left(a_m^{S,R} + a_m^{S2} \right) H_m^{(2)}(kr) + a_m^{I2} J_m(kr) \right) e^{im\theta}$$

(5)

where $a_m^{S,R}$ are the scattered radiated wave amplitudes as

before, a_m^{I2} are the incident wave amplitudes of the reflections off of the tank walls, beaches, and paddles. The amplitudes a_m^{S2} are the amplitudes of the scattering of the incident reflected waves. If one could find all of these coefficients, then the wave field including standing waves could be reproduced.

With only a single circle around which to measure, the outwardly propagating waves cannot be distinguished from the incoming reflections. This is completely analogous to the two-dimensional case where a single wave gauge cannot separate incident and reflected waves, while two or more wave gauges can. Similarly, if one had two concentric circles at radii r_0 and r_1, one could separate the outwardly propagating from the incoming waves by solving a system of equations:

$$\left(a_m^{S,R} + a_m^{S2}\right) H_m^{(2)}\left(kr_0\right) + a_m^{I2} J_m\left(kr_0\right)$$
$$= \frac{1}{2\pi} \int_{-\pi}^{\pi} \eta\left(r_0, \theta\right) e^{-\mathrm{i}m\theta} \quad (6)$$

$$\left(a_m^{S,R} + a_m^{S2}\right) H_m^{(2)}\left(kr_1\right) + a_m^{I2} J_m\left(kr_1\right)$$
$$= \frac{1}{2\pi} \int_{-\pi}^{\pi} \eta\left(r_1, \theta\right) e^{-\mathrm{i}m\theta} \quad (7)$$

For each m, the right-hand side is known, and one seeks the pair of unknowns: $\left(a_m^{S,R} + a_m^{S2}\right)$ and a_m^{I2}. However, the radiated wave or the primary scattered wave $(a_m^{S,R})$ still cannot be separated from the scattered waves due to reflections (a_m^{S2}). The locations of the zeros of the Bessel function must also be considered. To the authors' knowledge, such a method has not been proposed before.

The wave field that is measured around the circle includes both the outwardly propagating and inwardly propagating waves, and in the single circle method used herein, the Cylindrical coefficients are fitted to a model which assumes all wave energy is propagating outwardly. This means that if there is significant reflected energy present around the circle, the coefficients and resulting Cylindrical wave field will be inaccurate. This can be seen in Figure 10, which shows the scattered wave field of the Attenuator oriented at $45°$ in 1.25 Hz, and is the worst result from this study. There are significant standing waves shown along s1 and s2, and s4 shows a line of very high measurements that are not captured by the model.

It may be difficult to determine where the reflections are coming from, why the Attenuator at $45°$, 1.25 Hz, was the worst case, and why the spokes s1, s2, and s4 show such disagreement. Reflections propagated in all directions, but given the location of the standing waves, it may be that the reflections were from the wave paddles. Although the paddles were force feedback, they may not have been able to respond to the small amplitude of the scattered waves (< 1 cm).

The inability to distinguish incoming from outgoing waves is a flaw in the experimental design. Perhaps the two-circle design should have been used to determine reflections. However, other research being done suggests that these reflections would have very high m cylindrical values, which would be difficult to capture accurately from the circle of wave gauges. A better approach would be to minimize the reflected energy, perhaps with absorbing wave paddles and floating beach in a wave tank like FloWave [13].

Given the issues with higher-order harmonics and reflections, the results still show that a wave field represented by the cylindrical solutions is good approximation of the wave field produced by physical reality within the linear signal domain.

V. Conclusion

Experiments were conducted in The University of Edinburgh Curved Wave Tank to measure the cylindrical coefficients of the scattered and radiated wave fields of two different geometries of WECs at three different frequencies. The resulting cylindrical analytical wave fields were then compared to measurements at other points in the wave tank and with a cylindrical wave field created numerically with the BEM software WAMIT. The measured cylindrical wave field generally agreed very well with the measured wave field. The numerical wave field did not agree quite as well, and one reason for this was that there was energy at higher order components, which could not be modelled by WAMIT. Additionally, reflections of the scattered and radiated waves off of the wave tank paddles, walls, and beaches caused some inaccuracies in the derivation of the cylindrical coefficients, which proved to be more significant in some conditions than in others. Ultimately, the experiments have served as validation for the use of cylindrical wave fields for representing the scattered and radiated waves of floating bodies.

References

[1] M. Wypych, L. Le-Ngoc, K. Alexander, and A. Gardner, "On the application of circular-cylindrical waves to ocean wave power absorption," *Ocean Engineering*, vol. 40, pp. 69–75, Feb. 2012.

[2] J. C. McNatt, V. Venugopal, and D. Forehand, "A novel method for deriving the diffraction transfer matrix and its application to multi-body interactions in water waves," *Ocean Engineering*, vol. 94, pp. 173–185, Jan. 2015.

[3] H. Kagemoto and D. K.-P. Yue, "Interactions among multiple three-dimensional bodies in water waves: an exact algebraic method," *Journal of Fluid Mechanics*, vol. 166, pp. 189–209, 1986.

[4] R. Carballo and G. Iglesias, "Wave farm impact based on realistic wave-WEC interaction," *Energy*, vol. 51, pp. 216–229, Mar. 2013.

[5] C. Beels, P. Troch, G. De Backer, M. Vantorre, and J. De Rouck, "Numerical implementation and sensitivity analysis of a wave energy converter in a time-dependent mild-slope equation model," *Coastal Engineering*, vol. 57, no. 5, pp. 471–492, May 2010.

[6] A. Babarit, "On the park effect in arrays of oscillating wave energy converters," *Renewable Energy*, vol. 58, pp. 68–78, Oct. 2013.

[7] J. C. McNatt, V. Venugopal, and D. Forehand, "The Cylindrical Wave Field of Wave Energy Converters," in *Proc. of the 10th European Wave and Tidal Energy Conf., Aalborg, Denmark*, Aalborg, Denmark, 2013.

[8] ——, "The cylindrical wave field of wave energy converters," *International Journal of Marine Energy*, vol. 3-4, pp. e26–e39, Dec. 2013.

[9] J. N. Newman, *Marine Hydrodynamics*. MIT Press, 1977.

[10] I. Gyongy, J.-B. Richon, T. Bruce, and I. Bryden, "Validation of a hydrodynamic model for a curved, multi-paddle wave tank," *Applied Ocean Research*, vol. 44, pp. 39–52, Jan. 2014.

[11] J. Cruz, *Ocean Wave Energy: Current Status and Future Prospectives (Green Energy and Technology)*. Springer, 2008.

[12] F. John, "On the motion of floating bodies II," *Communications on Pure and Applied Mathematics*, vol. 3, pp. 45–101, 1950.

[13] "FloWaveTT," http://www.flowavett.co.uk/, accessed: 2015-06-15.